The Astronomical Journal, 166:23 (10pp), 2023 July https://doi.org/10.3847/1538-3881/acd92e
© 2023. The Author(s). Published by the American Astronomical Society.
OPEN ACCESS

Estimation of the Flux at 1450 MHz of OB Stars for FAST and SKA

Qichen Huang (黄启宸)[1,2], Biwei Jiang (姜碧沩)[1,2], Dingshan Deng (邓丁山)[3], Bin Yu (于斌)[4], and Albert Zijlstra[5]
[1] Institute for Frontiers in Astronomy and Astrophysics, Beijing Normal University, Beijing 102206, People's Republic of China; qchuang@mail.bnu.edu.cn, bjiang@bnu.edu.cn
[2] Department of Astronomy, Beijing Normal University, Beijing 100875, People's Republic of China
[3] Lunar and Planetary Laboratory, The University of Arizona, Tucson, AZ 85721, USA
[4] Songshan Lake Future School, Dongguan 523808, People's Republic of China
[5] Department of Physics and Astronomy, The University of Manchester, Manchester M13 9PL, UK
Received 2023 March 7; revised 2023 May 24; accepted 2023 May 24; published 2023 June 23

Abstract

Radio observation is crucial to understanding the wind mechanism of OB stars but very scarce. This work estimates the flux at 1450 MHz ($S_{1.4\mathrm{GHz}}$) of about 5000 OB stars identified by the LAMOST spectroscopic survey and confirmed by the Gaia astrometric as well as astrophysical measurements. The calculation is performed under the free–free emission mechanism for wind with the mass-loss rate derived from stellar parameters. The estimated $S_{1.4\mathrm{GHz}}$ distributes from 10^{-11} to 10^{-3} Jy with the peak at about 10^{-8} Jy. This implies that the complete SKA-II can detect more than half of them, and some tens of objects are detectable by FAST without considering source confusion. An array of FAST would increase the detectable sample by 2 orders of magnitude.

Unified Astronomy Thesaurus concepts: OB stars (1141); Radio continuum emission (1340); Stellar winds (1636); Radio telescopes (1360)

Supporting material: machine-readable table

1. Introduction

Massive OB stars usually have strong winds that produce a significant mass-loss rate on the order of 10^{-4}–$10^{-6}\,M_{\odot}\,\mathrm{yr}^{-1}$, which greatly influences the evolution of the star and the surrounding interstellar medium (Matthews 2018). Thanks to Castor et al. (1975), who described the theory of radiation-driven wind, we now have a basic understanding of how this kind of stellar wind is generated. However, there are still some important questions that radio observations can uniquely answer. First, in the strong stellar wind of OB stars, the dominant radio emission is considered to be the thermal free–free radiation from the ionized gas around the star. A big advantage of using radio flux to determine the mass-loss rate is that its radiation is generated farther away in the stellar wind than UV or X-ray radiation and can be considered to have almost reached its terminal velocity. Consequently, it has no strong dependence on the ionization environment, internal velocity field, etc., and the mass-loss rate can be determined more precisely. Moreover, stellar wind is dynamically unstable for OB stars, which leads to shock formation and clumping. This clumping will enhance the radio emission and produce variation in the spectral index as a function of frequency (Daley-Yates et al. 2016). The radio observation therefore provides unique insights into the nature of this stellar wind.

Radio observations of OB stars have been conducted by some groups. Isequilla et al. (2019) observed the Cygnus OB2 and OB8 regions by the Giant Metrewave Radio Telescope, and detected nine young massive stars that have the flux at 325 MHz and 610 MHz above 2 mJy. Previously, Kennedy et al. (2010) examined 50 observations across frequencies between 1.4 GHz and 43 GHz using the Very Large Array (VLA) to observe the Cygnus OB2 No.5 system. As a binary system with an OB star orbiting, its radio flux per observation exceeded 2.5 mJy. Their model derives a mass-loss rate of $3.4\times10^{-5}M_{\odot}\,\mathrm{yr}^{-1}$ for Cyg OB2 No. 5, which is unusually high for an Of supergiant and comparable to that of WR stars. On the other hand, the e-Merlin Cyg OB2 Radio Survey (COBRaS) project has accumulated about 300 hr of observations on 1000 OB stars in the Cygnus OB2 association at 5 GHz and 1.6 GHz (Willis et al. 2011). They reported that the 21 cm flux of O3 to O6 supergiant and giant stars is less than $\sim$70 μJy, which may imply an upper-limit mass-loss rate of $\sim4.5\times10^{-6}M_{\odot}\,\mathrm{yr}^{-1}$ for the O3 supergiants and $\leqslant2.9\times10^{-6}M_{\odot}\,\mathrm{yr}^{-1}$ for B0 to B1 supergiants.

The detection of OB star radio emission is generally difficult due to its weakness. With the development of large radio telescopes like FAST (Jiang et al. 2020) and planned big projects such as The Square Kilometre Array (SKA; Combes 2015), sensitivity is greatly increased, and the detection of a large number of OB stars becomes possible; consequently, the stellar wind mechanism and properties can be better understood. Recently, Yu et al. (2021) generated a star catalog that includes the OB stars through the Besançon model, and used this as a target to estimate the observability of the SKA Telescope. They reported that SKA can detect 1500 Be stars and 50 OB stars per square degree out to several kiloparsecs at the limit of 10 nJy at 5 GHz.

The FAST telescope is a pointing facility that cannot compare with the wide field of view (FOV) of SKA. In this regard, the catalog generated by the Besançon model cannot offer the positions of the real targets. The 500 m aperture in combination with the receiver's system temperature $<$30 K of FAST makes it one of the most sensitive telescopes at the decimeter wave bands currently available. The estimation of the radio flux of OB stars would provide suitable targets for studying the ionized wind. Synchronous with the development of radio astronomy, the sample of OB stars is significantly

Original content from this work may be used under the terms of the Creative Commons Attribution 4.0 licence. Any further distribution of this work must maintain attribution to the author(s) and the title of the work, journal citation and DOI.

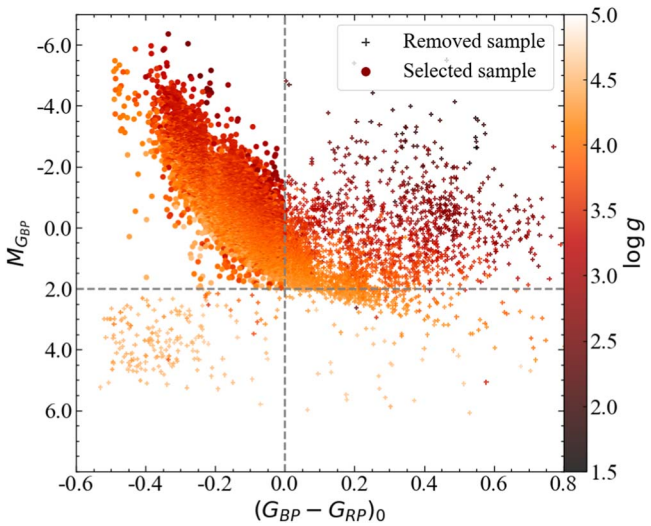

Figure 1. The color–magnitude diagram of all of the initial sample stars, among which the star kept in the final sample is denoted by dot and the removed star is denoted by cross. The color bar indicates the surface gravity.

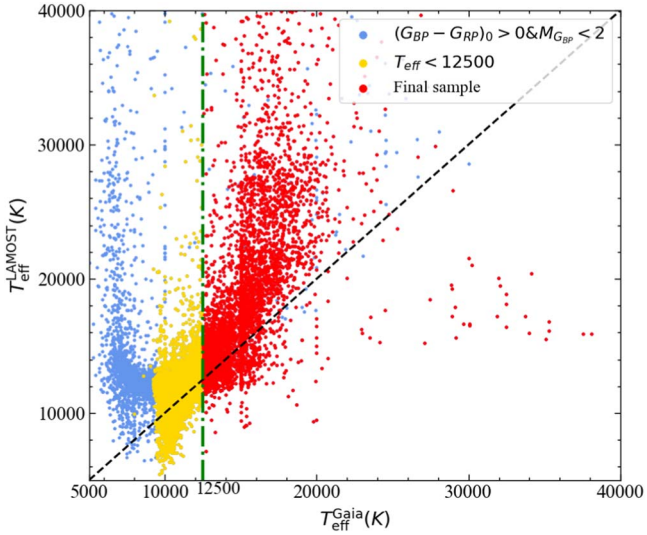

Figure 2. Comparison of $T_{\rm eff}$ derived by Gaia/DR3 and LAMOST. The blue dot denotes the objects we filtered out by $(G_{\rm BP} - G_{\rm RP})_0 > 0$ and $M_{G_{\rm BP}} < 2$. The yellow dot denotes the objects that pass photometry screening; however, $T_{\rm eff}$ is lower than 12,500 K and therefore removed as well. The red dot denotes the stars for which we finally calculate the radio flux.

augmented by large-scale optical spectroscopic surveys. The recent publication of the new OB star catalog by Guo et al. (2021) includes 16,032 early-type stars through measuring the equivalent widths of several absorption lines profiles using low-resolution spectra from the LAMOST database. In addition, the release of Gaia/DR3 data has brought us high-precision distance as well as stellar parameters and interstellar extinction. These data lead to the feasibility of predicting the detectability of OB stars by the large radio facilities based on the real stars instead of the model ones. It will also be helpful to identify the radio stars in the SKA large area observations.

This work intends to estimate the radio flux of a large sample of OB stars and then to predict observability by the FAST and SKA Telescopes. In brief, the initial sample of OB stars is taken from the catalog identified from the LAMOST optical spectrum. As it is a reflective Schmidt telescope with a diameter of 5 m and an FOV of 5° squared, LAMOST can provide spectra for about 4000 objects in one exposure and has accumulated spectra for nearly 10 million stars (Cui et al. 2012; Luo et al. 2015). This sample is further cleaned by the Gaia measurements. With the stellar parameters derived from Gaia, the mass-loss rate and the radio flux at 1450 MHz are estimated, to be compared with the visibility and sensitivity of the FAST and SKA telescopes in order to predict the number of observable objects. The data is presented in Section 2, the method in Section 3, and the results in Section 4.

2. The Sample

The initial sample is the OB star catalog of Guo et al. (2021), who used the Stellar LAbel Machine (SLAM), which is a machine-learning method, to screen the spectra taken by LAMOST. They identified 578 and 3931 OB stars within the training parameters from the LAMOST medium-resolution spectra (MRS) and low-resolution spectra (LRS), respectively, and calculated their effective temperature $T_{\rm eff}$, surface gravity log g, metallicity [Fe/H], etc. For the stars outside the parameters' range, they calculated the atmospheric parameters by extrapolation from SLAM. Adding this part from extrapolation, Guo et al. (2021) built up a catalog of 9287 and 22,292 OB stars from LAMOST/MRS and LRS, respectively. After removing the duplicate sources while keeping the result from the highest signal-to-noise ratio spectrum, the total number of sources becomes 21,731. This catalog is the first one that comprises consistently derived stellar labels for such a large sample of early-type stars (Guo et al. 2021).

This initial sample is further cleaned by using the Gaia/DR3 data. For hundreds of millions of stars, Gaia/DR3 provides stellar parameters with a method called the General Stellar Parameterizer from Photometry (GSP-Phot), including effective temperature, surface gravity, metallicity, absolute magnitude, radius, distance, and extinction, with the information from astrometry, and photometric and low-resolution BP/RP spectra (Andrae et al. 2022). We first look up the location of the initial sample stars in the color–magnitude diagram to confirm that the object is an early-type star. The extinction is taken from the Gaia extinction measurements through Gaia's low-resolution BP/RP spectroscopy, which have been validated in several places, such as the Sun-like stars project of Creevey et al. (2022). Delchambre et al. (2022) proved that the overall extinction map of the Milky Way drawn by Gaia/DR3 is in good agreement with the Planck data and with the SFD98 2D extinction map (Schlegel et al. 1998). In this step, the sources whose extinction is unavailable in the Gaia/DR3 catalog are rejected, which leaves 13,729 sources in the sample. For the distance, the geometric distance of Gaia/EDR3 given by Bailer-Jones et al. (2021) is adopted and available for all of the sources.

The color–magnitude diagram, $(G_{\rm BP} - G_{\rm RP})_0$ versus $M_{G_{\rm BP}}$, of the stars in the initial sample is presented in Figure 1. The stars can be mainly divided into three groups. One group of stars has an absolute magnitude $M_{G_{\rm BP}}$ fainter than 2 mag, which disagrees with the brightness of OB stars. Meanwhile, their intrinsic color index $(G_{\rm BP} - G_{\rm RP})_0$ is mostly <0, indicating a high temperature. These are probably hot subdwarf stars. The fact that their surface gravity denoted by the color in Figure 1 is generally >4.5 supports the subdwarf classification. Another group of stars has an intrinsic color index $(G_{\rm BP} - G_{\rm RP})_0 > 0.2$, which is apparently redder than the OB

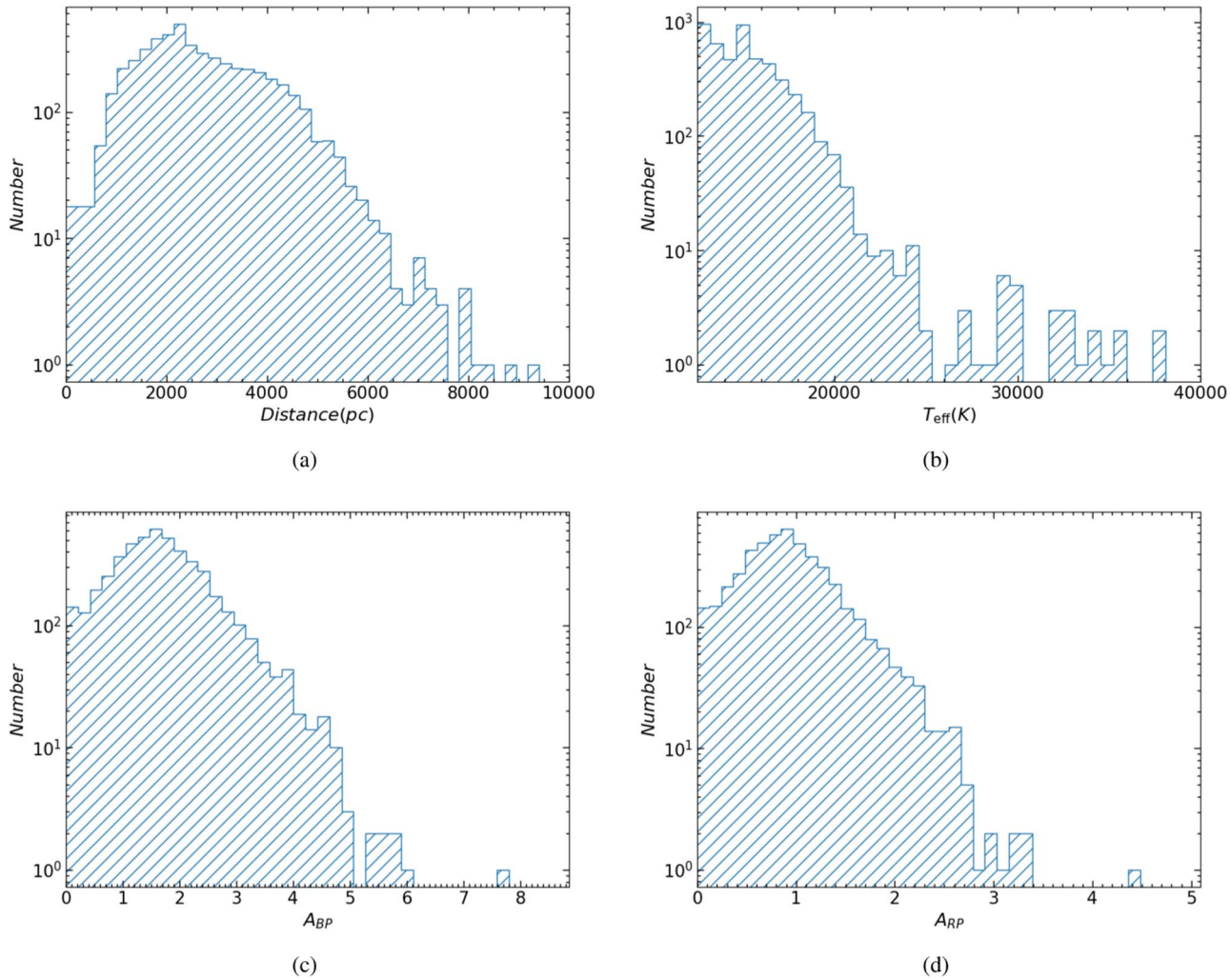

Figure 3. Histogram of distance, effective temperature, and interstellar extinction in the Gaia/BP and RP band of the sample stars.

stars, and they may be giant stars considering their $M_{\rm G_{BP}}$ brighter than 0 mag. Their relatively small surface gravity, $\log g < 2.5$, supports their classification as giant stars. These two groups of stars are excluded. Consequently, the left sample contains 10,646 stars, which coincide with OB stars in color, brightness, and surface gravity.

3. Calculation of Stellar Parameters

The estimation of radio flux needs several stellar parameters, including distance, luminosity, mass, and effective temperature, in combination with other parameters.

3.1. Distance, Extinction, and Effective Temperature

As mentioned above, the distance is taken from the geometric distance of Gaia/EDR3 given by Bailer-Jones et al. (2021). On the effective temperature, both Gaia and LAMOST give the values. Gaia/GSP-Phot yielded very good results, with half of the values being within 170 K of those in the literature. In comparison with the effective temperature in the LAMOST catalog in Figure 2, the value from GSP-Phot does not differ much from LAMOST in the range of 10,000–15,000 K, which is the most numerous part of the catalog. Meanwhile, the GSP-Phot temperature is significantly lower than that of LAMOST in the ranges of 5000–10,000 K and 15,000–20,000 K. Although the Gaia/DR3 temperature may be overestimated for some stars due to the overestimated extinction by GSP-Phot (Andrae et al. 2022), we still choose the Gaia/DR3 temperature instead of the LAMOST temperature. This is because the Gaia/DR3 parameters are far more significantly consistent between the parameters (effective temperature, surface gravity, and absolute magnitude) than LAMOST. Furthermore, Guo et al. (2021) was aware that the stellar parameters from the extrapolation are not highly reliable. This can be attributed to the additional constraint from the distance by Gaia. Consequently, 3915 stars in the initial LAMOST sample have a Gaia effective temperature smaller than 10,000 K and are dropped from further analysis. The stars with $T_{\rm eff} \in$ 10,000–12,500 K are also dropped because no appropriate calculation can be made for their mass-loss rates to be described later. Consequently, the extinction is retrieved from the Gaia/DR3 catalog. The histogram of these parameters is shown in Figure 3.

3.2. Luminosity and Mass

The luminosity is calculated using the bolometric correction (BC) for the Gaia blue band $G_{\rm BP}$. Pedersen et al. (2020) derived the formulae to calculate the BC to the hot magnitude from stellar effective temperature $T_{\rm eff}$, surface gravity $\log g$, and metallicity (optional). Andrae et al. (2022) pointed out that the metallicity results of Gaia/DR3 have a large systematic

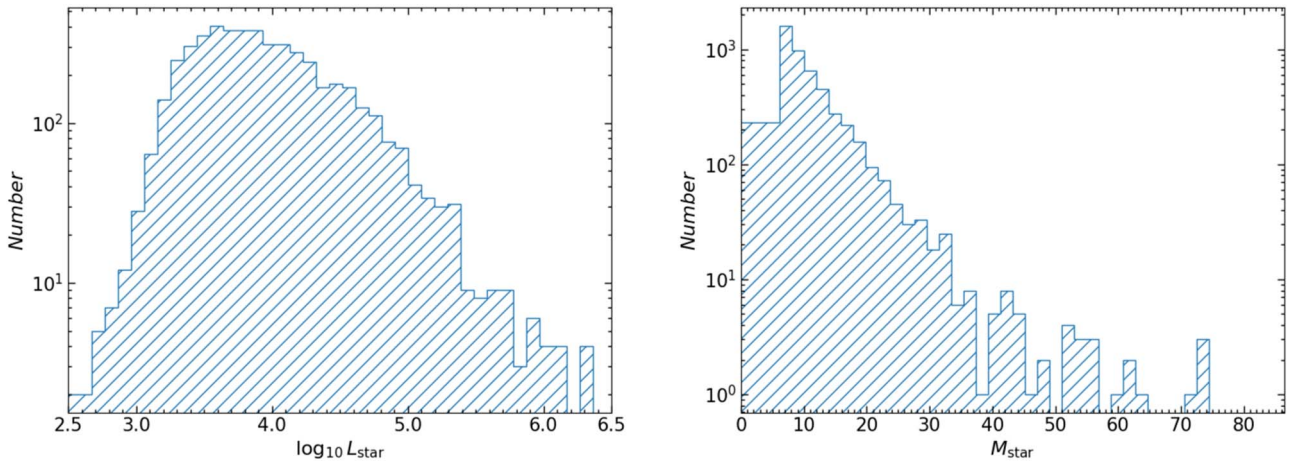

(a) (b)

Figure 4. Histogram of luminosity and mass of the sample stars.

uncertainty and thus are not recommended. Therefore, we choose a function of only $T_{\rm eff}$ and $\log g$ as follows:

$$BC = \beta_0 + \beta_1 x_1 + \beta_2 x_1^2 + \beta_3 x_1^3 + \beta_4 x_2 + \beta_5 x_2^2, \quad (1)$$

where $x_1 = \log_{10} T_{\rm eff}/T_{\rm eff,0}$ with $T_{\rm eff,0} = 10{,}000$K, $x_2 = \log g$, and β_0, β_1, $\cdots$,β_5 are constants. For the $G_{\rm BP}$ band, β_0, β_1, $\cdots$,β_5 are -0.3021, -5.1276, -0.1952, 0.0000, and 0.0836, respectively.

The apparent bolometric magnitude $m_{\rm bol}$ is then calculated from $G_{\rm BP}$ taking the above BC and the interstellar extinction $A_{G_{\rm BP}}$ into account:

$$m_{\rm bol} = G_{\rm BP} + BC - A_{G_{\rm BP}}, \quad (2)$$

which is converted to luminosity with distance.

The mass–luminosity relation of Eker et al. (2015) is used to calculate the mass from the luminosity. Eker et al. (2015) divided the stellar mass into four groups, namely, low mass, intermediate mass, high mass, and very high mass with $M/M_\odot$ in the ranges of 0.38–1.05, 1.05–2.40, 2.4–7.0, and 7.0–32, respectively. Since the OB stars are massive, only the mass–luminosity relations for high mass and very high mass are adopted as follows:

$$\begin{aligned} \log_{10} L &= 3.962 \log_{10} M - 0.120 \ (2.4 \leqslant M/M_\odot \leqslant 7) \\ \log_{10} L &= 2.726 \log_{10} M + 1.237 \ (7 \leqslant M/M_\odot \leqslant 32). \end{aligned} \quad (3)$$

The preliminary mass calculation eliminated 106 stars with $M < 2.4 M_\odot$. Because the mass–luminosity relation of Eker et al. (2015) is based on mass rather than luminosity, the calculation is iterated. First, the mass is calculated from the luminosity by the relation for high-mass stars, and for the stars whose calculated masses exceed the range of high mass, i.e., $> 7M_\odot$, the mass is recalculated by the mass–luminosity relation for the very-high-mass stars. Due to the gap in luminosity between the high-mass and the very high-mass relations, 560 stars obey neither of the two relationships. However, since neither the mass nor the difference calculated by the two relations has much influence on the radio flux, we directly used the relation of very-high-mass stars for these 560 sources to calculate their masses.

The stars whose calculated mass is greater than $32M_\odot$ are not rejected. Although the mass of these sources may be greatly overestimated, they are definitely more massive than $30M_\odot$, with the highest one close to $90M_\odot$. This level of overestimation is significantly diluted in our mass-loss rate equation and will bring about a difference less than an order of magnitude. Moreover, such stars are supposed to be the most luminous sources with the highest radio flux. The histograms of the luminosity and mass are shown in Figure 4.

3.3. Mass-loss Rate

Mass-loss rate ($\dot{M}$) is a key parameter to estimate the radio flux. We calculate $\dot{M}$ with the formula developed by Vink et al. (2000), which used the Monte Carlo method to fit the mass-loss rate of OB-type stars as the function of stellar luminosity, mass, and effective temperature. The core idea of this method is that the total energy of the radiation is related to the total momentum gained by the outflowing matter, and the momentum in the stellar wind can be calculated from the action history of the large number of photons released below the photosphere. The specific calculation method of mass-loss rate is divided into the high-temperature and low-temperature groups due to the "bi-stability jump" effect around 25,000 K (Yu et al. 2021).

In the higher-temperature range of 27,500–50,000 K, $\dot{M}$ in units of $M_\odot\,{\rm yr}^{-1}$ is given by:

$$\begin{aligned} \log_{10}\dot{M} &= -6.697 + 2.194 \log_{10}(L_\star/10^5 L_\odot) \\ &- 1.313 \log_{10}(M_\star/30M_\odot) - 1.226 \log_{10}\left(\frac{v_\infty/v_{\rm esc}}{2.0}\right) \\ &+ 0.933 \log_{10}(T_{\rm eff}/40{,}000{\rm K}) - 10.92 \log_{10}(T_{\rm eff}/40{,}000{\rm K})^2. \end{aligned} \quad (4)$$

In the lower-temperature range of 12,500–22,500 K, it is

$$\begin{aligned} \log_{10}\dot{M} = &-6.688 + 2.210 \log_{10}(L_\star/10_\odot^5) \\ &- 1.339 \log_{10}(M_\star/30M_\odot) \\ &- 1.601 \log_{10}\left(\frac{v_\infty/v_{\rm esc}}{2.0}\right) \\ &+ 1.07 \log_{10}(T_{\rm eff}/20{,}000{\rm K}). \end{aligned} \quad (5)$$

According to the work of Lamers et al. (1995), the value of the ratio $v_\infty/v_{\rm esc}$ is 2.6 for the higher temperature and 1.3 for the lower temperature. It can be seen that the lowest

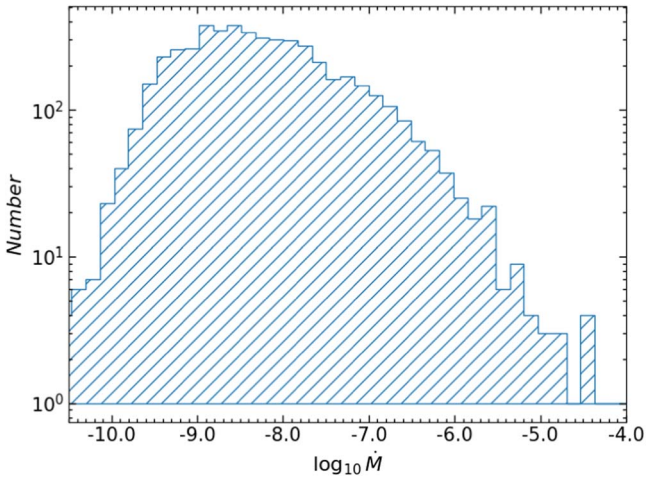

Figure 5. Histogram of the mass-loss rate.

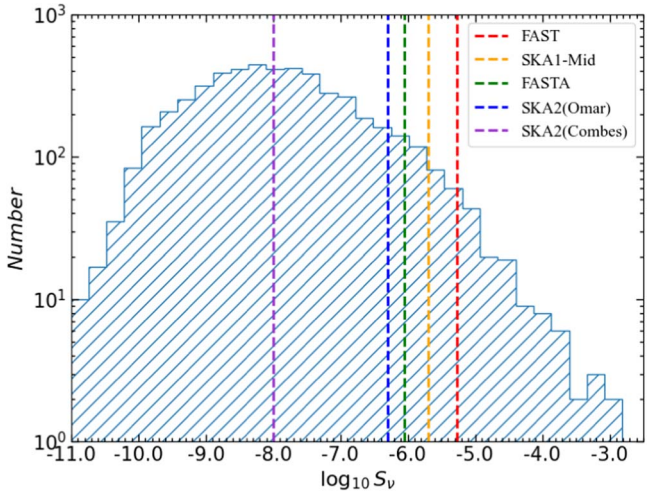

Figure 6. Histogram of the calculated $S_{1.4\mathrm{GHz}}$, where the sensitivity of FAST/FASTA/SKA is marked by the dashed lines. The two sensitivities of SKA2 come from Omar (2023) and Combes (2015), respectively.

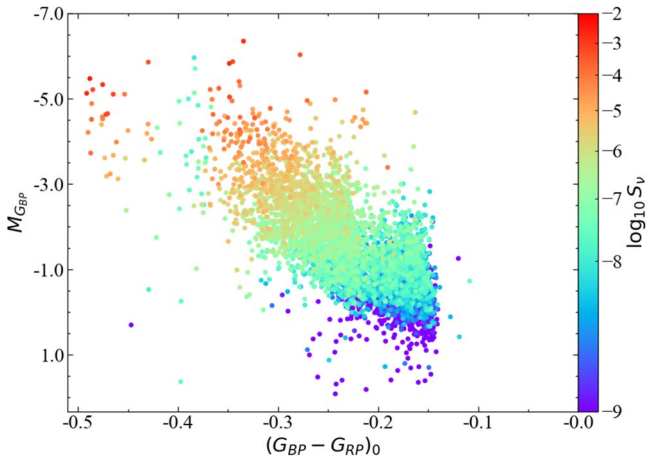

Figure 7. The distribution of the calculated $S_{1.4\mathrm{GHz}}$ in the color–magnitude diagram of the sample stars.

temperature in Equation (5) is 12,500 K, which implies that stars with lower temperatures would have an insignificant mass-loss rate. Therefore, we further remove the stars with $T_{\mathrm{eff}} < 12{,}500$ K, which leads to the final sample of 4930 stars with mass-loss rate and radio flux calculated, which is about a quarter of the initial sample.

It can be seen that the formulae lack an effective temperature range between 22,500 and 27,500 K. This is due to the existence of the bi-stability jump effect, and no reliable algorithm is available for calculating $\dot{M}$ in this T_{eff} range in Vink et al. (2000). Nevertheless, since about 2% of the sample stars are in this range, we still estimate their $\dot{M}$ by a simple linear interpolation between the two sides of the high- and low-temperature ends as follows:

$$\dot{M} = -3.832 \times 10^{-13} T_{\mathrm{eff}} + 1.966 * 10^{-8}. \quad (6)$$

This calculation may be not accurate, but it is tolerable as $\dot{M}$ itself bears large uncertainty. The current typical mass-loss rate algorithms have factors of 2–3 uncertainty (Matthews 2018).

The distribution of the yielded $\dot{M}$ is shown in Figure 5. The peak mass-loss rate is around 10^{-9}–$10^{-8} M_\odot\,\mathrm{yr}^{-1}$, which is 3 orders of magnitude higher than 10^{-12}–$10^{-11} M_\odot\,\mathrm{yr}^{-1}$ derived in Yu et al. (2021). This difference is mainly caused by different temperature distributions. In Yu et al.'s (2021) calculations, the temperature of the source simulated using the Basancon model was concentrated around 10,000 to 12,500 K, while the sources in this work are mostly above 12,500 K. The higher temperature implies higher luminosity and higher $\dot{M}$. There are 97 sources with $\dot{M} > 10^{-6} M_\odot\,\mathrm{yr}^{-1}$.

4. Radio Flux

4.1. The Result

According to the classical spectral line-driven stellar wind theory, the radio emission of OB stars originates from the thermal free–free radiation of ionized gas around the star resulting from mass loss (Wright & Barlow 1975; Lamers et al. 1999; Vink 2011). The flux density S_ν in units of millijanskys at a frequency ν in gigahertz in the radio band is related to the mass-loss rate $\dot{M}$ in $M_\odot\,\mathrm{yr}^{-1}$ under the assumption of spherically symmetric uniform wind as follows: (Panagia & Felli 1975; Wright & Barlow 1975)

$$S_\nu = \frac{2.30 \times 10^7 \dot{M}^{4/3} Z^{4/3} (\gamma g_{\mathrm{ff}} \nu)^{2/3}}{\mu^{4/3} v_\infty^{4/3} D^2}, \quad (7)$$

where μ is the average ion weight, v_∞ is the terminal velocity in kilometer per second, D is the distance in kiloparsecs, Z is the effective charge per ion, γ is the average number of electrons per ion, and g_{ff} is the free–free Gunter factor given by:

$$g_{\mathrm{ff}} = -1.66 + 1.27 \lg(T_{\mathrm{wind}}^{3/2}/(Z\nu)) \quad (8)$$

where T_{wind} is the temperature of the radio photosphere layer.

We assume that the stellar wind of OB stars is completely ionized, and we take the cosmic abundance of elements, which gives Z, γ, and μ values of 1, 1, and 1.26, respectively. The observation frequency is set to be 1450 MHz, the terminal velocity is 1000 km s^{-1}, and T_{wind} is set to be 0.5 T_{eff} (Lamers & Leitherer 1993; Abbott et al. 1981). The flux at other frequency can be calculated from $S_{1450\mathrm{MHz}}$ by the relation of $S_\nu \propto \nu^{0.67}$.

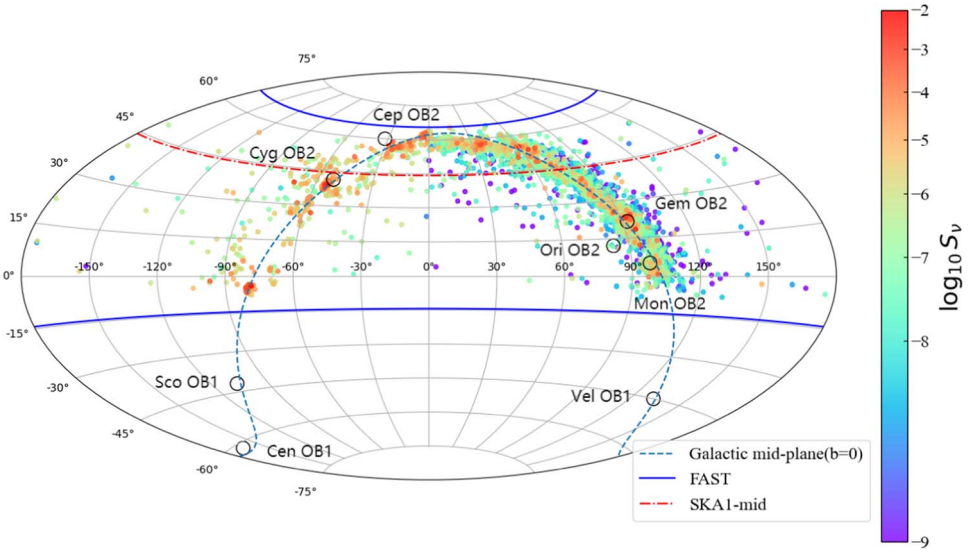

Figure 8. The spatial distribution of the sample stars in the equatorial coordinate, where the Galactic plane is denoted by blue dashed line, and the latitude limit of FAST and SKA1-mid is denoted by blue solid line and red dashed line, respectively. Several famous OB associations are labeled.

Table 1
The $S_{1.4\mathrm{GHz}}$ Brightest OB Stars

R.A. (°)	Decl. (°)	Distance pc	G_{BP}	G_{RP}	$A_{G_{\mathrm{BP}}}$	$M_{G_{\mathrm{BP}}}$	$C^0_{G_{\mathrm{BP}},G_{\mathrm{RP}}}$	T_{eff} 10^4 K	L_{star} $10^5 L_\odot$	M_{star} $M_\odot$	$\dot{M}$ $10^{-6} M_\odot\ \mathrm{yr}^{-1}$	Flux mJy
55.1326	50.7481	2596	11.6	10.27	4.0	−4.65	−0.47	3.41	9.9	56	7.5	0.156
101.2242	0.6202	4109	9.34	8.67	2.08	−6.03	−0.28	1.74	8.0	51	16.9	0.172
69.2314	53.876	3966	11.33	10.0	3.9	−5.86	−0.43	2.96	19.8	72	16.0	0.181
306.7926	38.9004	1732	10.92	9.48	4.27	−4.63	−0.47	3.21	9.2	54	5.6	0.237
94.8142	12.1818	6203	12.63	11.5	3.57	−5.21	−0.49	4.09	21.6	74	38.3	0.244
95.0133	24.2293	4218	10.47	9.5	2.91	−5.87	−0.35	2.01	8.7	53	22.8	0.248
88.1402	25.7641	3085	11.56	10.22	4.03	−5.1	−0.46	3.4	14.6	64	14.5	0.266
36.0093	57.3539	2154	9.28	8.48	2.53	−5.04	−0.35	2.05	5.0	43	8.9	0.271
64.5241	53.6187	3847	12.39	10.82	4.57	−5.33	−0.48	3.75	21.8	74	35.2	0.563
60.2266	55.2278	3757	10.52	9.19	3.72	−6.35	−0.33	1.95	13.1	62	44.5	0.760
92.4183	23.0729	3302	10.58	9.74	2.9	−5.13	−0.49	4.05	21.5	74	37.6	0.840
281.3574	−4.0169	2818	11.37	9.63	4.72	−5.83	−0.35	2.14	10.2	56	32.2	0.884
94.9165	18.3715	3423	10.58	9.64	3.11	−5.47	−0.49	4.1	28.8	82	62.9	1.550

Note. The full version of the $S_{1.4\mathrm{GHz}}$ catalog is available in machine-readable form. This portion only shows the brightest OB stars. The full catalog contains 4930 stars and includes additional columns of information.

(This table is available in its entirety in machine-readable form.)

The histogram of the calculated flux is displayed in Figure 6. The peak of the distribution is at about 10^{-8} Jy. In comparison, this value is 10^{-13} Jy in Yu et al. (2021), i.e., 5 orders of magnitude lower. The above calculation indicates that the peak of mass-loss rate distribution in the present work is 3 orders of magnitude higher and would lead to a higher radio flux by 4 orders of magnitude. The other order can be attributed to the distance with its peak being at about 2 kpc for the present sample, a few factors closer than that (∼5 kpc) in Yu et al. (2021). Moreover, the Besancon model that Yu et al. (2021) used is a virtual model that contains no real stars. It is a model for the galaxy that is populated by creating stars so that it fits the expected distribution. This also explains the difference with Yu et al. (2021); the Besancon model does not include clusters and, therefore, misses the clustering of the most-massive stars, but is dominated by the less-massive yet much more common stars.

It is worth mentioning that, according to Vink et al. (2000), there are two peaks of the mass-loss rate of stars at ∼20,000 K and ∼40,000 K, respectively. In the range from 22,500 to 27,500 K, stellar mass-loss rate decreases rapidly with increasing temperature, and at around 27,500 K, the mass-loss rate of the stars is similar to that of stars at around 12,500 K. Therefore, we can clearly see in Figure 7 that there are a number of sources with very small S_ν, at the position of $(G_{\mathrm{BP}} - G_{\mathrm{RP}})_0 = -0.37$ to -0.4 that corresponds to a temperature between 22,500 and 27,500 K. The sources with very high S_ν are concentrated between $(G_{\mathrm{BP}} - G_{\mathrm{RP}})_0 = -0.35$ and -0.5, corresponding to temperatures of ∼20,000 K and ∼40,000 K.

4.2. The Spatial Distribution

The distribution of the sources is displayed in Figure 8 with the radio flux denoted by the color bar. As expected from their young age, massive stars are mostly distributed near the Galactic plane, with high flux sources concentrated within the plane. However, there are some outlying sources beyond the

Galactic plane, although they have relatively low fluxes. It should be noted that the radius of the circle in the figure is not proportional to the size of the actual sky area of the OB association. When comparing with the nearby OB associations assembled by Ruprecht (1966), a few are apparently matched, such as Mon OB2, Gem OB2, and Cyg OB2, meanwhile, Ori OB2 and Cep OB2 are not well matched. Furthermore, a few OB associations are beyond the survey area covered by LAMOST. On the other hand, some clusters of OB stars were not in the early list of OB associations. This mismatch may be caused by the incomplete sky coverage of the LAMOST survey.

4.3. The Sample Detectable by FAST and SKA

The sensitivity of FAST is calculated at the frequency of 1450 MHz with a system temperature of 30 K (Jiang et al. 2020). With an on-source integration time of 30 minutes and a bandwidth of 200 MHz, the sensitivity is approximately 10 μJy at the 5σ level. As shown in Figure 6, the flux of 82 stars, or 1.62% of the total sample, is above this level. On the other hand, the very high sensitivity leads to confusion that is about 1 mJy for the continuum observation. By taking the confusion limit into account, only five stars are detectable. However, the uncertainty in the estimated radio flux is significant, originating from the uncertain mass-loss rate as well as the model of the wind. Therefore, the brightest OB stars are still potential objects with the thermal wind emission detectable by FAST. In Table 1, we listed the brightest 13 stars with $S_\nu > 0.1$ mJy in the sample, which deserves an attempt by FAST.

The estimated observing power of SKA1-mid is based on the performance given by Braun et al. (2019), who calculated that its point-source sensitivity would be 2 μJy within an integration time of 1 hr. For the sensitivity of SKA2, Braun et al. (2019) stated that it is still uncertain. However, from the overall telescope configuration, the performance of SKA2 is about 20 times that of SKA1. Therefore, Omar (2023) cited Braun et al. (2019) and gave 0.5 μJy as a reference value. We also use this value as the sensitivity of SKA2 for comparison.With this sensitivity, there would be 392 stars detectable by SKA1-mid and 749 stars detectable by SKA2. In Figure 6, we also plotted the estimated maximum observational capability of SKA2 by Combes (2015) as a reference cited by Yu et al. (2021), who calculated that the point-source sensitivity would be close to 10 nJy within an integration time of 8 hr.

The observable sky area of FAST and SKA1-mid is marked as well in Figure 8. The geographical latitude of FAST telescope is 25.°6 north, and its meridian-like structure can move within the zenith angle $< 40°$, so its observable range is between $-14.°4$ and $65.°6$ in decl., which is marked by the blue line in Figure 8. Because the LAMOST telescope locates at a latitude of 40°, nearly all of the sources are within the FAST observable area. On the other hand, SKA will be located in the southern hemisphere. If we take an elevation of 15° above the horizon as the limit, its observable sky area is south of 44.3° N in decl., which is marked by the red line in Figure 8. Due to the large difference in geographical latitude of SKA with LAMOST, many of the candidate sources are beyond the SKA sky. Taking the SKA's location into account, only part of the object is visible to SKA1-mid, which reduces the number of detectable stars from 392 to 174.

A plan in China to build an FAST array (FASTA) is under discussion. For example, an array of six 500 m telescopes with more advanced receivers would not only increase the sensitivity by nearly an order of magnitude, but also alleviate the problem of confusion of a single dish. Such a facility would be very powerful in detecting radio emission of stars. In the case of OB stars, the number of stars detectable would be 583, which is several tens of times the present performance of FAST.

5. Discussion

5.1. The Cyg OB2 Association

The COBRaS project has observed 1000 OB stars in the Cygnus OB2 association for a total of about 300 hr at 5 GHz and 1.6 GHz (Willis et al. 2011). According to Morford et al. (2017), two O stars (Cyg OB2 #7 and A15) and one B star (Cyg OB2 #12) have model-predicted flux $S_{1.4\mathrm{GHz}}$ of 20.5, 16.7, and 1770 μJy, respectively, but only Cyg OB2 #12 is detected with $S_{1.4\mathrm{GHz}} = 341$ μJy, significantly lower than the predicted. Meanwhile, the two O stars are not detected and have an upper limit of 150 and 138 μJy, respectively. By detailed study of four O stars and five B stars observed in this project, Morford et al. (2016) inferred the upper limit of mass-loss rate from the nondetection at 1.4 GHz for four O stars and four B stars to be smaller than $5 \times 10^{-6} M_\odot\,\mathrm{yr}^{-1}$, which is in general agreement with the model within 1 order of magnitude. For Cyg OB2 #12, the only detected source, they derived $\dot{M}$ to be $5.4 \times 10^{-6} M_\odot\,\mathrm{yr}^{-1}$ from $S_{1.4\mathrm{GHz}} = 1013$ μJy, which is about one-fifth of the model predicted $24.5 \times 10^{-6} M_\odot\,\mathrm{yr}^{-1}$. The multiepoch observations indicate that the radio flux of Cyg OB2 #12 is variable, and there is significant discrepancy between the observation and the model prediction.

In comparison with our predicted mass-loss rate, Morford et al. (2016) used the same mass-loss rate model (Vink et al. 2000). However, Morford et al. (2016) used the specific values of stellar luminosity and mass for its nine observation targets cited from Clark et al. (2012) and other five papers, which are different from our calculations. For the nine stars in Morford et al. (2016), most of them in our results have much lower effective temperatures. Since these stars are mostly in the main sequence, the lower effective temperature leads to smaller luminosity, mass, and mass-loss rate. On the other hand, for stars whose effective temperature and surface gravity are close to the observed targets of Morford et al. (2016), their masses exceed 32 solar masses in our estimation. Due to our mass algorithm, the estimated mass of these stars may be overestimated already. When comparing with the observation results of Morford et al. (2016), this overall impact means that there may be an overestimation of the radio flux of stars with the largest mass.

According to Knodlseder (2000), Cyg OB2 is centered at about R. A. $= 20^{\mathrm{h}}33^{\mathrm{m}}10^{\mathrm{s}}$ and decl. $= +41°12'$ (J2000) with an angular diameter of about 2°. Berlanas et al. (2019) showed that the Cyg OB2 has two structures at a distance of $\sim$1.76 kpc and $\sim$1.35 kpc, respectively. Fourteen stars in our sample are located within this area and listed in Table 2, two of which are very possibly beyond the distance range of the association. Unfortunately, the members mentioned above are not included in the sample. Instead, the sample stars are generally much fainter, and the estimated $S_{1.4\mathrm{GHz}}$ is on the order of a microjansky.

Table 2
OB Stars in the Cyg OB2 Range

R.A. (°)	Decl. (°)	Distance pc	G_{BP}	G_{RP}	$A_{G_{BP}}$	$M_{G_{BP}}$	$C^0_{G_{BP},G_{RP}}$	T_{eff} 10^4 K	L_{star} $10^4 L_\odot$	M_{star} $M_\odot$	$\dot{M}$ $10^{-9} M_\odot$ yr^{-1}	Flux 10^{-3} mJy
306.7644	40.0505	977	11.26	10.7	1.65	−0.42	−0.19	1.39	0.3	7	1.1	0.016
307.7038	40.7569	1295	12.57	11.61	2.67	−0.69	−0.24	1.5	0.5	8	2.5	0.029
308.4219	41.5515	1242	11.66	10.86	2.19	−1.13	−0.18	1.34	0.6	8	2.5	0.031
307.3004	40.5779	1697	12.55	11.26	3.31	−2.0	−0.18	1.25	1.1	11	7.8	0.074
305.7393	40.7336	1677	13.58	12.06	4.0	−1.57	−0.24	1.51	1.2	11	10.4	0.114
309.7769	41.6833	1347	13.95	12.12	4.75	−1.51	−0.25	1.5	1.1	11	8.7	0.139
308.5251	40.718	1243	12.76	11.27	3.91	−1.66	−0.24	1.5	1.3	11	11.6	0.239
307.1527	40.6245	1539	12.03	10.82	3.2	−2.24	−0.22	1.42	1.8	13	19.1	0.303
310.1077	41.6242	1277	13.67	11.58	5.35	−2.24	−0.24	1.5	2.2	14	29.1	0.776
306.9336	41.5497	1284	9.92	9.64	1.2	−1.87	−0.28	1.74	2.1	13	31.5	0.867
307.3386	39.9884	1647	12.44	10.95	3.9	−2.66	−0.24	1.53	3.1	16	54.2	1.071
306.9359	40.4274	1732	12.85	11.15	4.4	−2.79	−0.24	1.5	3.5	16	66.9	1.28
308.0163	39.8207	1330	16.04	12.68	8.44	−3.17	−0.23	1.5	4.5	18	103.5	3.885
306.1209	40.6174	2208	12.65	10.93	4.43	−3.61	−0.24	1.5	7.1	21	222.8	3.917

Table 3
Objects Cross-matched with the NVSS Catalog by a Radius of 15″

Source Name	σ^{NVSS}_{RA} (″)	σ^{NVSS}_{Decl} (″)	Distance (pc)	T_{eff} 10^4K	M_{star} $M_\odot$	L_{star} $10^3 L_\odot$	$\dot{M}$ $10^{-10} M_\odot$ yr^{-1}	S^{NVSS}_ν mJy	$S^{this\ work}_\nu$ mJy	$Flag^{45''}_{SIMBAD}$
stellar sources										
TYC 2440-341-1	0.05	0.7	1718	1.3	5	1.1	1.2	29.8	2.8×10^{-7}	A
SDSS J062231.18+262932.4	0.3	3.6	3996	1.4	6	2.1	4.3	4.1	2.8×10^{-7}	A
TYC 3661-1648-1	0.2	1.8	1720	1.3	7	3.6	11.7	9.5	5.8×10^{-6}	A
Gaia DR3 4422493164360011 52	0.25	2.4	1909	1.5	10	8.1	53.8	6.2	3.7×10^{-5}	B
TYC 154-1153-1	0.04	0.6	1665	.6	9	7.8	54.3	53.9	4.9×10^{-5}	C
MFJ SH 2-272 3	0.13	1.6	3476	1.7	14	21.1	311.0	12.4	1.2×10^{-4}	C
BD+54 3	0.22	2.0	2784	2.0	22	76.6	3479.0	9.1	4.6×10^{-3}	A
nonstellar										
NVSS J055708+210742	0.04	0.6	2885	1.3	6	1.7	2.6	71.5	2.7×10^{-7}	
Lan 76	0.57	9.6	4438	1.6	16	34.3	672.5	2.5	2.0×10^{-4}	
NVSS J061453+122122	0.03	0.6	3254	1.7	19	56.7	1725.7	329.6	1.3×10^{-3}	
unidentified										
NVSS 065159+135744	0.17	2.4	4958	1.3	6	1.9	3.2	5.9	1.3×10^{-7}	
NVSS J062542.25+195956.0	0.57	8.9	3548	1.6	9	6.2	36.2	13.1	6.3×10^{-6}	
NVSS J195848+404205	0.04	0.6	4645	1.4	10	10.1	71.7	755.6	$9.0 \cdot 10^{-6}$	

Note. They are divided into three classes by the SIMBAD database: the first part as stellar sources, the second part as nonstellar sources, and the third part as unidentified. The stellar sources are further divided into three groups according to the situation within a 45″ circle: they are marked as "A" if there is no objects, marked as "B" if there are other stars, and marked as "C" if there are other radio sources.

5.2. Cross-match with the NVSS Catalog

The sample stars are cross-matched with the NRAO VLA Sky Survey (NVSS) Catalog (Condon et al. 1998). The NVSS Catalog covers the sky north of the decl. of −40° at 1.4 GHz, identical with the area of the sample and the frequency in calculation. It includes a catalog of almost 2 million discrete sources brighter than a flux density of about 2.5 mJy. The rms uncertainties in R.A. and decl. are ∼7″ at the survey limit, which is the expected value of the OB stars. By taking a radius of 15″ for cross-identification, a total of 13 sources are found.

These 13 objects are queried through the SIMBAD database for their classification. It is found that they belong to three categories: seven confirmed stellar objects, three confirmed nonstellar objects, and three unidentified, which are listed in Table 3. Their estimated fluxes in this work are generally several orders of magnitude below the NVSS sensitivity. It seems they are false matches. Therefore, a further examination for all confirmed stellar objects is performed. The SIMBAD data is searched within a 45″ range near each source, and the results are presented in Table 3. Within the 45″ area, four sources are marked as "A" because there are no objects, and one source is marked as "B" because there are other stars or uncertain data that could influence the result, and two sources are marked as "C" because there are clear radio source(s). It can be assumed that the cross-identification is unreliable if there are other sources within this range, i.e., the Class B and C sources.

5.3. The Influence of Binary

Early-type stars have a high binary rate. In early-type binary stars, if both stars are OB stars or WR stars, their strong stellar winds will collide and produce extremely strong nonthermal synchrotron radiation. This nonthermal synchrotron radiation is usually considered to be produced by relativistic particles. Since the radio photosphere of these early-type stars is approximately hundreds of stellar radii, if the binary star is wide (with a period $>$ 10 yr), then nonthermal synchrotron radiation will be

produced outside the radio photosphere of the star. If the period of the binary star is < 1 yr, then nonthermal synchrotron radiation from the wind collision region will not be observable because it will be absorbed in the optically thick region of the individual star's wind (Eichler & Usov 1993; Van Loo et al. 2008; De Becker & Raucq 2013; De Becker et al. 2017).

Luo et al. (2021) used the data from LAMOST/DR5 to derive a binary probability of $0.4^{+0.05}_{-0.06}$ for OB stars. Here, we take the selection method used by Guo et al. (2022) to find the binaries in our sample. Guo et al. (2022) calculated the radial velocity of 9382 early-type stars in the LAMOST medium-resolution survey data in the Guo et al. (2021) table and identified binaries according to the velocity dispersion with the following criteria:

$$\frac{|v_i - v_j|}{(\sigma_i^2 + \sigma_j^2)^{\frac{1}{2}}} > 4$$
$$|v_i - v_j| > C, \quad (9)$$

where v_i and σ_i are the radial velocity and the associated uncertainty measured for the spectrum at epoch i(j), respectively. In order to eliminate pulsating variables, the constant C is set to 15.57 km s^{-1} (Guo et al. 2022).

According to this criteria, 95 of the 559 objects with the radial velocity measurements in our sample are binaries, i.e about 17%. This fraction is smaller than the 40% derived by Luo et al. (2021). Due to the lack of specific parameters about the binary orbits, we cannot further determine the binary contribution to the radio flux. However, it is certain that the radio flux of some binaries would be increased by the wind interaction. On the other hand, the measurement of radio flux may become an indicator of a binary. Based on Van Loo et al.'s (2008) observation of Cyg OB2 No.9's radio flux at 6 cm wavelength using VLA, they thought that the thermal synchrotron radiation of this binary was 2 mJy, and the nonthermal synchrotron radiation varied between 0 and 6 mJy with a period of 2.35 yr. Taking this as reference, we estimate that if the binaries in our data are double early-type stars, their nonthermal synchrotron radiation will increase their radio flux by up to three times. If their companions are not OB stars or WR stars with high mass-loss rates, then their radio flux will remain unchanged.

5.4. The Effects of Clumping

The stellar wind of OB stars exhibits dynamic instability, which leads to the formation of shocks and clumps. These clumps enhance radio emission and cause the spectral index α to vary with frequency. Williams et al. (1990) found a significant deviation from $\alpha = 0.6$ at high frequencies in their study of Wolf–Rayet star γ Velorum at submillimeter and infrared frequencies. Nugis et al. (1998) found that the winds of WN and WC stars exhibit steepening phenomena in the spectrum with $\alpha = 0.77$ and 0.75, respectively, deviating from $\alpha = 0.6$ due to clumping of stellar wind material.

Daley-Yates et al. (2016) used the Atacama Large Millimeter/submillimeter Array to study the effect of clumping on spectral index α within the range of 10–10^4 GHz. The results showed that clumping would cause the spectral index α to rise from the standard 0.6 to between 0.7 and 0.8 when the frequency is below 500 GHz. The spectral index α used in our radio flux calculation formula was 2/3 (0.66). According to Daley-Yates et al.'s (2016) results, we take 0.6 and 0.8 as the minimum and maximum values of the spectral index α, respectively, under the clumping effect. It is evident from Equation (7) that the influence of spectral index variations in the range of 0.6–0.8 on the radio flux S_ν is weak. A change in α from 0.66–0.6 results in a decrease of 2.3% in the flux, while a change in α from 0.66–0.8 will result in an increase of 4.5% in the flux. Even if we take the extreme case that $\alpha = 2.0$, the flux would be increased by 57%, still within a factor of 2.

6. Summary

Based on the Guo et al. (2021) OB star catalog and the newly published Gaia/DR3 stellar parameters, we quantitatively calculated and analyzed the radio flux of OB stars in the catalog to estimate whether they are likely to be detected by FAST and SKA. We conducted further screening of the OB stellar candidates listed in Guo et al. (2021), and separated out the hot subdwarfs, main-sequence OB stars, and giant stars through the color–magnitude diagram. The mass-loss rate is derived from stellar parameters, which are then used to estimate the apparent flux at 1450 MHz under the assumption of free–free emission mechanism with stellar distance.

The mass-loss rate of about 4930 OB stars ranges from about 10^{-4} to $10^{-11} M_\odot$ yr^{-1}, and correspondingly, the flux at 1.4 GHz ranges from 10^{-3} to 10^{-11} Jy. The high-flux stars are distributed mostly in the Galactic plane, as expected for massive stars. By comparing with the sensitivity and considering the sky coverage, 82 objects are detectable by FAST if confusion is neglected. However, this number would only be 5, if confusion is taken into consideration. So employment of an FAST array would be extremely helpful for detecting such pointlike stellar sources and important to understand stellar wind and evolution. For the SKA, there will be 392 and 749 stars detectable by SKA1-mid and SKA2, respectively.

We estimated the binary proportion in our source table. Ninety-five out of the 559 objects in our sample with radial velocity measurements are binaries, i.e., about 17%. Assuming the extreme case that the binary probability for the entire population is higher, at 40%, and that all binaries are double early-type stars with triple the flux, the number of observable sources for FAST, SKA1-mid, and SKA2 would increase to 124, 504, and 919, respectively, with an increase of 42, 112, and 170 sources.

We are grateful to Drs. Mengyao Xue, Yanjun Guo, and Jing Tang for their helpful discussion. The authors are grateful to the anonymous referee, whose comments helped to improve this work significantly. This work is supported by the NSFC project 12133002, National Key R&D Program of China No. 2019YFA0405503, and CMS-CSST-2021-A09. This work has made use of the data from LAMOST and Gaia.

ORCID iDs

Qichen Huang (黄启宸) https://orcid.org/0000-0002-4046-2344
Biwei Jiang (姜碧沩) https://orcid.org/0000-0003-3168-2617
Dingshan Deng (邓丁山) https://orcid.org/0000-0003-0777-7392
Bin Yu (于斌) https://orcid.org/0000-0003-1178-5176
Albert Zijlstra https://orcid.org/0000-0002-3171-5469

References

Abbott, D. C., Bieging, J. H., & Churchwell, E. 1981, ApJ, 250, 645
Andrae, R., Fouesneau, M., Sordo, R., et al. 2022, arXiv:2206.06138

Bailer-Jones, C., Rybizki, J., Fouesneau, M., Demleitner, M., & Andrae, R. 2021, AJ, 161, 147
Berlanas, S., Wright, N., Herrero, A., Drew, J., & Lennon, D. 2019, MNRAS, 484, 1838
Braun, R., Bonaldi, A., Bourke, T., Keane, E., & Wagg, J. 2019, arXiv:1912.12699
Castor, J. I., Abbott, D. C., & Klein, R. I. 1975, ApJ, 195, 157
Clark, J. S., Najarro, F., Negueruela, I., et al. 2012, A&A, 541, A145
Combes, F. 2015, JInst, 10, C09001
Condon, J. J., Cotton, W., Greisen, E., et al. 1998, AJ, 115, 1693
Creevey, O., Sordo, R., Pailler, F., et al. 2022, arXiv:2206.05864
Cui, X.-Q., Zhao, Y.-H., Chu, Y.-Q., et al. 2012, RAA, 12, 1197
Daley-Yates, S., Stevens, I., & Crossland, T. 2016, MNRAS, 463, 2735
De Becker, M., Benaglia, P., Romero, G. E., & Peri, C. S. 2017, A&A, 600, A47
De Becker, M., & Raucq, F. 2013, A&A, 558, A28
Delchambre, L., Bailer-Jones, C., Bellas-Velidis, I., et al. 2022, arXiv:2206.06710
Eichler, D., & Usov, V. 1993, ApJ, 402, 271
Eker, Z., Soydugan, F., Soydugan, E., et al. 2015, AJ, 149, 131
Guo, Y., Li, J., Xiong, J., et al. 2022, RAA, 22, 025009
Guo, Y., Zhang, B., Liu, C., et al. 2021, ApJS, 257, 54
Isequilla, N. L., Fernández-López, M., Benaglia, P., Ishwara-Chandra, C., & del Palacio, S. 2019, A&A, 627, A58
Jiang, P., Tang, N.-Y., Hou, L.-G., et al. 2020, RAA, 20, 064
Kennedy, M., Dougherty, S., Fink, A., & Williams, P. 2010, ApJ, 709, 632
Knodlseder, J. 2000, arXiv:0007442
Lamers, H. J., Cassinelli, J. P., & Cassinelli, J. 1999, Introduction to stellar winds (Cambridge: Cambridge Univ. Press), doi:10.1017/CBO9781139175012
Lamers, H. J., & Leitherer, C. 1993, ApJ, 412, 771
Lamers, H. J., Snow, T. P., & Lindholm, D. M. 1995, ApJ, 455, 269
Luo, A.-L., Zhao, Y.-H., Zhao, G., et al. 2015, RAA, 15, 1095
Luo, F., Zhao, Y.-H., Li, J., Guo, Y.-J., & Liu, C. 2021, RAA, 21, 272
Matthews, L. D. 2018, PASP, 131, 016001
Morford, J., Fenech, D., Prinja, R., Blomme, R., & Yates, J. 2016, MNRAS, 463, 763
Morford, J., Prinja, R., & Fenech, D. 2017, in IAU Symp. 316, Formation, Evolution, and Survival of Massive Star Clusters (Cambridge: Cambridge Univ. Press), 169
Nugis, T., Crowther, P., & Willis, A. 1998, A&A, 333, 956
Omar, A. 2023, JApA, 44, 1
Panagia, N., & Felli, M. 1975, A&A, 39, 1
Pedersen, M. G., Escorza, A., Pápics, P. I., & Aerts, C. 2020, MNRAS, 495, 2738
Ruprecht, J. 1966, BAICz, 17, 33
Schlegel, D. J., Finkbeiner, D. P., & Davis, M. 1998, ApJ, 500, 525
Van Loo, S., Blomme, R., Dougherty, S., & Runacres, M. 2008, A&A, 483, 585
Vink, J. S. 2011, Ap&SS, 336, 163
Vink, J. S., de Koter, A., & Lamers, H. J. 2000, A&A, 362, 295
Williams, P., Van Der Hucht, K., Sandell, G., et al. 1990, MNRAS, 244, 101
Willis, A., Prinja, R., & Fenech, D. 2011, Bulletin de la Société Royale des Sciences de Liège, 80, 524, https://popups.uliege.be/0037-9565/index.php?id=3029
Wright, A. E., & Barlow, M. J. 1975, MNRAS, 170, 41
Yu, B., Zijlstra, A., & Jiang, B. 2021, Univ, 7, 119